

Highlights

Adapting Medical Vision Foundation Models for Volumetric Medical Image Segmentation via Active Learning and Selective Semi-supervised Fine-tuning

Jin Yang, Daniel S. Marcus, Aristeidis Sotiras

- We propose an Active Selective Semi-supervised Fine-tuning (ASSFT) method to adapt medical vision foundation models to target evaluation domains in volumetric medical image segmentation. This method integrates a novel Active Test Time Sample Query strategy and a Selective Semi-supervised Fine-tuning approach.
- We propose an Active Test Time Sample Query strategy to select informative samples to fine-tune medical vision foundation models. This strategy employs two novel query metrics, termed Diversified Knowledge Divergence (DKD) and Anatomical Segmentation Difficulty (ASD).
- We propose a Selective Semi-supervised Fine-tuning method to further fine-tune medical vision foundation models by leveraging a small number of unannotated samples.
- We implemented extensive experiments to evaluate the effectiveness of our ASSFT method on five volumetric medical image segmentation tasks. Our method outperformed other state-of-the-art AL and ADA methods.

Adapting Medical Vision Foundation Models for Volumetric Medical Image Segmentation via Active Learning and Selective Semi-supervised Fine-tuning

Jin Yang^a, Daniel S. Marcus^a and Aristeidis Sotiras^{a,b,***}

^a*Mallinckrodt Institute of Radiology, Washington University School of Medicine in St. Louis, St. Louis, 63110, MO, USA*

^b*Institute for Informatics, Data Science and Biostatistics, Washington University School of Medicine in St. Louis, St. Louis, 63110, MO, USA*

ARTICLE INFO

Keywords:

Vision Foundation Models
Domain Adaptation
Active Learning
Semi-supervised Learning
Medical Image Segmentation

ABSTRACT

Medical vision foundation models (Med-VFMs) have been effectively developed for interpreting medical images due to the knowledge learned from self-supervised pre-training with extensive unannotated images. To improve their performance on downstream tasks, particularly segmentation, a small number of target-domain samples are often selected randomly for fine-tuning. However, random selection may fail to identify the most informative samples, limiting Med-VFMs' adaptation performance. Therefore, an efficient method for fine-tuning Med-VFMs by selecting informative samples is highly desirable. To address this, we propose an Active Selective Semi-supervised Fine-tuning (ASSFT) method to efficiently adapt Med-VFMs to target domains for volumetric medical image segmentation. Our approach employs a novel Active Learning (AL) strategy to select the most informative target-domain samples for fine-tuning without requiring access to source pre-training data, maximizing performance under a minimal selection budget. In this AL method, we design an Active Test Time Sample Query strategy to select samples from the target domain via two query metrics: Diversified Knowledge Divergence (DKD) and Anatomical Segmentation Difficulty (ASD). DKD measures the source-target knowledge gap and intra-domain diversity. It utilizes the knowledge from pre-training to guide the querying of source-dissimilar and semantic-diverse samples from the target domains. ASD evaluates the segmentation difficulty of anatomical structures by adaptively measuring predictive entropy in foreground regions, allowing the selection of samples with high information content in regions of interest rather than across the entire sample. Additionally, after fine-tuning by AL-queried samples, our ASSFT method employs a Selective Semi-supervised Fine-tuning to further improve the adaptation performance. It selects a specific ratio of unqueried samples, and combine them with AL-queried samples to further fine-tune Med-VFMs in a semi-supervised manner. We adapted Med-VFMs to five domains for volumetric medical image segmentation using our method to demonstrate its effectiveness. Our method achieved superior performance on these tasks than other active learning and active domain adaptation methods.

1. Introduction

Medical visual foundation models (Med-VFMs) have been developed for interpreting medical imaging and have demonstrated impressive ability in various medical image analysis tasks (Zhang and Metaxas, 2024). Med-VFMs typically employ convolutional neural networks or vision transformers as basic architectures and are pre-trained on diversified unannotated imaging data via self-supervised learning (Moor et al., 2023; Zhou et al., 2023; Pai et al., 2025; Wang et al., 2025; Zhu et al., 2025). Once trained, these models can be applied directly to perform tasks as they are (i.e., non-adaptive tasks) or they might form the backbone that will be adapted for specific downstream tasks (i.e., adaptive tasks). When they are applied to non-adaptive tasks for zero-shot predictions, they demonstrate remarkable performance due to the intrinsic knowledge learned from pre-training. In contrast, when they are employed for downstream evaluation of adaptive tasks, including classification and segmentation, their zero-shot performance is low. For example, when Med-VFMs are employed for segmenting target organs in unseen

domains, they are incorporated with a newly initialized decoder with the symmetric architecture to generate an encoder-decoder segmentation network. Thus, this segmentation network has not been fine-tuned to capture target extrinsic features via fully supervised training, and thus it is not capable to accurately recognize extrinsic patterns of target organs.

To boost the performance of Med-VFMs on adaptive downstream evaluation, especially segmentation, some samples from target evaluation domains are selected for fine-tuning, equipping Med-VFMs with the capabilities of recognizing extrinsic target patterns. Random selection is usually implemented to achieve it (Pai et al., 2025). However, fine-tuning Med-VFMs by randomly selecting samples may be suboptimal since it is not possible to ensure that informative samples have been selected. To address this limitation, active learning (AL) can be implemented to iteratively optimize the model by selecting the most informative samples at each iteration, thus maximizing the model performance using the minimum number of samples (Settles, 2011). AL methods are employed to query informative samples by designing different query strategies to evaluate the predictive uncertainty and sample diversity (Siddiqui et al., 2020; Wu et al., 2021; Xie et al., 2022; Li et al., 2023a; Yang et al., 2024).

***Corresponding author

 aristeidis.sotiras@wustl.edu (A. Sotiras)

ORCID(s):

Active domain adaptation (ADA) methods implement AL to adapt models across domains by utilizing query strategies to select the most informative samples from target domains for optimizing models (Ning et al., 2021; Du and Li, 2023; Zhang et al., 2024).

However, applying AL and ADA methods to actively adapt Med-VFMs to target domains in downstream tasks has three limitations. First, these methods lack mechanisms to query the most informative samples by leveraging the knowledge learned from pre-training. However, evaluating the sample informativeness by leveraging the pre-training knowledge from Med-VFMs facilitates the quantification of unlearned knowledge in target domains, thus improving the adaptation performance and efficiency. Second, these methods employ query strategies to evaluate information levels on the whole images or volumes. However, measuring image-level informativeness of target samples may misestimate their information levels due to the imbalance between foreground and background regions. Organs of interest cover a small part of the image compared with background. Thus, evaluating sample-level information levels leads these methods to query samples with a high information level in the background while under-estimating the information level of foreground organs. Thus, these methods cannot query samples with informative foreground patterns for fine-tuning, limiting Med-VFMs from capturing organ-related target features. Third, ADA methods rely on data from source domains for querying (Mahapatra et al., 2024), but source data or their annotations used for pre-training Med-VFMs are unavailable, thus limiting the applicability of these methods. Strict data privacy regulations in clinical practice may limit query strategies from accessing source data. Although some active source-free domain adaptation (ASFDA) techniques are proposed to adapt models to target domains without access to the source data (Wang et al., 2023; Li et al., 2023b), their performance is challenged by the first two limitations.

Employing AL or ADA methods to query samples from target domains to fine-tune Med-VFMs may boost their performance. However, this approach ignores large amount of target domain samples that lack annotations. To improve the performance of fine-tuning, some semi-supervised learning methods have been proposed and incorporated into ADA methods (Wang et al., 2024a, 2022; He et al., 2024). These methods leverage the fine-tuned networks to generate pseudo-labels for all unlabeled samples, and then use both labeled samples and all unlabeled samples with their pseudo-labels to further fine-tune the networks. However, utilizing all unannotated samples with their pseudo labels for semi-supervised fine-tuning has two drawbacks. First, networks have not fully captured extrinsic patterns from target domains in the first several AL iterations, so they will generate low-quality pseudo-labels for some unannotated samples. Therefore, using them for fine-tuning may lead Med-VFMs to learn inaccurate patterns, lowering performance. Second, the relative ratio of queried samples to unannotated samples is small, so unannotated samples with their pseudo labels

may be dominating the objective function, thus hindering the network from learning from the queried samples and their annotations.

To tackle these limitations, we propose a novel **Active Selective Semi-supervised Fine-tuning** (ASSFT) method to adapt Medical Vision Foundation Models to target domains for volumetric medical image segmentation. This method employs a novel active learning method to query the most informative target samples for fine-tuning without requiring access to the source pre-training, thus maximizing the performance of Med-VFMs using a small number of queried samples. It also employs a **Selective Semi-supervised Fine-tuning** strategy to select reliable unqueried samples and use them to further fine-tune Med-VFMs. The proposed AL method employs an **Active Test Time Sample Query** strategy to select the most informative target samples based on two novel query metrics jointly, termed **Diversified Knowledge Divergence** (DKD) and **Anatomical Segmentation Difficulty** (ASD). DKD aims to query samples with unlearned knowledge on target domains from pre-training and intra-domain semantic diversity. Specifically, DKD calculates Prior and Adaptive Knowledge Divergence to measure knowledge gaps between source pre-training and target adapting domains by identifying source-dissimilar samples. It also evaluates intra-domain diversity during querying by penalizing samples which demonstrate large semantic similarity within the domain. Additionally, ASD evaluates the difficulty in segmentation of anatomical structures by measuring predictive entropy in foreground region of interest. The predictive entropy in foreground region is calculated based on the fine-tuning status adaptively. Thus, querying samples by ASD to fine-tune Med-VFMs enables them to capture unlearned knowledge from samples with complex anatomical structures, thereby achieving more accurate segmentation.

Additionally, the proposed Selective Semi-supervised Fine-tuning strategy allows the efficient fine-tuning by leveraging labeled and a specific number of selected unlabeled samples, thus improving adaptation performance over fully-supervised fine-tuning. Specifically, after fine-tuning Med-VFMs with samples queried from AL in a full-supervised manner, we select a specific ratio of unannotated samples with high reliability instead of utilizing all unannotated samples. Specifically, our strategy is to select samples with the highest confidence in their predictive probabilities and the smallest semantic distance to queried samples. This is because the models are more likely to generate high-quality pseudo labels for them. Incorporating these samples with high-quality pseudo-labels alongside the actively selected samples in the semi-supervised fine-tuning facilitates further refinement of Med-VFMs, leading to improved performance and generalization.

To demonstrate the effectiveness of our ASSFT method, we evaluated it by adapting Med-VFMs to five domains in volumetric medical image segmentation. These domains have large variations in imaging modalities, the number of structures to be segmented, and the number of samples. Our

method performed better than other state-of-the-art AL and ADA methods on these five domain adaptation tasks. Our contributions can be summarized as follows:

- We propose an Active Selective Semi-supervised Fine-tuning (ASSFT) method to adapt medical vision foundation models to target evaluation domains in volumetric medical image segmentation. This method integrates a novel Active Test Time Sample Query strategy and a Selective Semi-supervised Fine-tuning approach.
- We propose an Active Test Time Sample Query strategy to select informative samples to fine-tune medical vision foundation models. This strategy employs two novel query metrics, termed Diversified Knowledge Divergence (DKD) and Anatomical Segmentation Difficulty (ASD).
- We propose a Selective Semi-supervised Fine-tuning method to further fine-tune medical vision foundation models by leveraging a small number of unannotated samples.
- We implemented extensive experiments to evaluate the effectiveness of our ASSFT method on five volumetric medical image segmentation tasks. Our method outperformed other state-of-the-art AL and ADA methods.

2. Related Works

2.1. Active Learning in Medical Image Segmentation

Active learning has been applied to achieve efficient training of medical image segmentation models by identifying the most informative samples to optimize models with the minimal annotation cost. A framework termed suggestive annotation has been designed for fine-tuning fully convolutional networks by using uncertainty and similarity information to determine the most representative and uncertain samples for labeling (Yang et al., 2017). Bayesian U-Net utilizes Monte Carlo dropout in active learning to select samples with the largest uncertainty for annotation (Hiasa et al., 2019). In a related approach, a query-by-committee framework was proposed to estimate uncertainty by multiple models (Nath et al., 2020). A deep active semi-supervised learning framework, DSAL, was proposed to select informative samples with high uncertainties and low uncertainties for strong labeling and weak labeling to efficiently utilize model knowledge for medical image segmentation (Zhao et al., 2021). A hybrid active learning framework was proposed to utilize a sample selection strategy to query samples for annotation by measuring pixel entropy, regional consistency and image diversity jointly (Li et al., 2023c). Active learning with stochastic batches was proposed to query batches by evaluating batch-level uncertainty and employing sampling with randomness for efficient medical image segmentation (Gaillochet et al., 2023). On the other

hand, SBC-AL employed an efficient query strategy to select samples with large uncertainty in the consistency of anatomical structure and boundary regions during active learning (Zhou et al., 2024). An active learning method is proposed to query representative samples based on image similarity for skin lesion segmentation (Shu et al., 2025).

2.2. Active Source-Free Domain Adaptation in Medical Image Analysis

A few active source-free domain adaptation methods have been proposed for medical image analysis, including classification and segmentation. An Active Learning with Feature Disentanglement and Domain Adaptation was proposed to query representative samples based on domain specific and task specific image features for annotation in medical image classification (Mahapatra et al., 2024). A Source-domain and Target-domain Dual-Reference (STDR) strategy was proposed for the segmentation of nasopharyngeal carcinoma tumors from Magnetic Resonance (MR) images across multiple domains (Wang et al., 2024a). This strategy was designed to actively select representative domain-invariant and domain-specific samples for annotations by utilizing references to demonstrate the distributional characteristics of the source domain and the target domain. Additionally, an uncertainty-guided method was proposed to adapt segmentation networks to different domains in prostate segmentation from MR images (Luo et al., 2024). This method actively selected samples with high uncertainty and diversity by employing a Global Aleatoric Uncertainty Aggregation strategy to estimate slice-wise uncertainty and k-means to group diverse samples. ASFDA was utilized for vessel segmentation from ultra-wide-field scanning laser ophthalmoscopy (UWF-SLO) images (Wang et al., 2024b). In this adaptation task, after the whole UWF-SLO image was split into patches, patches with high foreground certainty were selected actively for annotation by implementing a Cascade Uncertainty-Predominance Selection strategy. A novel Guided Attention Transfer Network (GATN) along with an active learning optimization strategy were employed to adapt models for classification, segmentation, and detection (Kothandaraman et al., 2023). A framework was proposed to adapt segmentation models across different domains and modalities by measuring image-level uncertainty and organ-level diversity (Yang et al., 2025).

2.3. Medical Vision Foundation Models

Several foundation models have been developed to interpret medical images with different modalities. Specifically, generalist medical AI was built using self-supervision on large medical data with diverse modalities (Moor et al., 2023). RETFound was developed as a foundation model for retinal images (Zhou et al., 2023). CT-FM was developed as a large-scale 3D image-based CT foundation model using label-agnostic contrastive learning and a large number of CT images (Pai et al., 2025), while FM-CT was pre-trained as a vision foundation model on head CT images using self-supervised learning for generalizable disease diagnosis (Zhu

Algorithm 1 Active Selective Semi-supervised Fine-tuning of Medical Vision Foundation Models

Input: Pre-trained encoder $E^{(p)}(\mathbf{X}_s)$; Initialized decoder $D^{(0)}$; Samples from unlabeled target domain $\mathbb{T} = \{\mathbf{X}_t\} = \{x_1, \dots, x_t, \dots, x_{N_t}\}$; Maximum AL round \mathcal{R} ; Query budget \mathcal{N}_B ; Total query budget \mathcal{N}_{AL} ; Selected unlabeled sample budget \mathcal{N}_{SU} .

Output: target-optimized Med-VFM-based segmentation network $\mathcal{F}(\Theta^*)$.

Begin:

- 1: Let current round $r = 0$;
- 2: Construct $\mathcal{F}(\Theta) \leftarrow \mathcal{F}^{(0)}(\Theta; [E^{(p)}; D^{(0)}])$ as the segmentation network;
- 3: Initialize $\mathbb{T}_l \leftarrow \emptyset$, $\mathbb{T}_u \leftarrow \mathbb{T}$;
- 4: **while** $r \leq \mathcal{R}$ **do**
- 5: **if** $r == 0$ **then**
- 6: Select x_1 and annotate y_1 from \mathbb{T} to optimize $\mathcal{F}(\Theta)$ as $\mathcal{F}^{(0)}(\Theta)$;
- 7: Update $\mathbb{T}_l \leftarrow \mathbb{T}_l \cup \{(x_1, y_1)\}$, $\mathbb{T}_u \leftarrow \mathbb{T}_u \setminus \{x_1\}$;
- 8: Continue;
- 9: **end if**
- 10: Calculate DKD(x_u) on samples x_u from \mathbb{T}_u by Eq. 5;
- 11: Calculate ASD(x_u) on samples x_u from \mathbb{T}_u by Eq. 11;
- 12: Calculate $Q(x_u)$ by Eq. 16;
- 13: Query \mathcal{N}_B samples \mathbf{X}_t^r with the largest scores for annotation \mathbf{Y}_t^r by manual annotators;
- 14: Update $\mathbb{T}_l \leftarrow \mathbb{T}_l \cup \{(\mathbf{X}_t^r, \mathbf{Y}_t^r)\}$, $\mathbb{T}_u \leftarrow \mathbb{T}_u \setminus \{\mathbf{X}_t^r\}$;
- 15: Fine-tune the network as $\mathcal{F}^{(r)}(\Theta)$ using \mathbf{X}_t^r with their annotations \mathbf{Y}_t^r from \mathbb{T}_l ;
- 16: Select \mathcal{N}_{SU} unlabeled samples $\mathbf{X}_{t,u}^r$ from \mathbb{T}_u by Eq. 26;
- 17: Generate pseudo labels $\mathbf{Y}_{t,u}^r$ for $\mathbf{X}_{t,u}^r$ by $\mathcal{F}^{(r)}(\Theta)$;
- 18: Update $\mathbb{T}_{l,p} \leftarrow \mathbb{T}_l \cup \{(\mathbf{X}_{t,u}^r, \mathbf{Y}_{t,u}^r)\}$;
- 19: Fine-tune the network $\mathcal{F}^{(r)}(\Theta)$ using $\mathbb{T}_{l,p}$;
- 20: $r \leftarrow r + 1$;
- 21: **end while**

End

et al., 2025). Triad was pre-trained as a 3D MRI foundation model (Wang et al., 2025).

3. Methods

3.1. Overall Methods

Without loss of generality, let us assume we have access to a medical vision foundation model that has been pre-trained using self-supervised learning on an extensive number \mathcal{N}_s of unannotated images \mathbf{X}_s from a specific modality \mathcal{M}_s forming the source domain $\mathbb{S} = \{\mathbf{X}_s\} = \{x_1, x_2, \dots, x_{\mathcal{N}_s} | \mathcal{M}_s\}$. To evaluate the Med-VFM on downstream adaptive segmentation tasks, the pre-trained Med-VFM is employed as an encoder E , and incorporated with

a symmetric decoder D into a U-shaped architecture, generating the segmentation model $\mathcal{F}(\Theta; [E; D])$. This segmentation model is evaluated on unlabeled data from a target domain via fine-tuning. This target domain \mathbb{T} includes \mathcal{N}_t images \mathbf{X}_t of the modality \mathcal{M}_t : $\mathbb{T} = \{\mathbf{X}_t\} = \{x_1, x_2, \dots, x_{\mathcal{N}_t} | \mathcal{M}_t\}$.

As shown in Algorithm 1, the goal of the Active Selective Semi-supervised Fine-tuning is to boost the performance of the Med-VFM-based segmentation model on the target data \mathbf{X}_t without access to the source data \mathbf{X}_s . During downstream evaluation, the ASSFT method implements active learning to fine-tune the pre-trained Med-VFM-based segmentation network. This AL procedure is implemented to fine-tune the network iteratively for \mathcal{R} rounds, and it employs a novel Active Test Time Sample Query strategy to select a small number \mathcal{N}_B of informative samples from the target domain \mathbb{T} for annotation during test time at each round. Thus, the total number of queried samples is $\mathcal{N}_{AL} = \mathcal{N}_B \cdot \mathcal{R}$ ($\mathcal{N}_{AL} << \mathcal{N}_t$). These queried samples with their annotation are utilized to fine-tune the segmentation network, thus improving its evaluation performance on this domain with the minimal number of query samples.

During initialization, the encoder is built from the pre-trained Med-VFM as $E^{(p)}(\mathbf{X}_s)$, and the decoder is newly initialized as $D^{(0)}$ with a symmetric architecture. Thus, the network $\mathcal{F}(\Theta)$ is constructed as $\mathcal{F}(\Theta; [E^{(p)}(\mathbf{X}_s); D^{(0)}])$. All images in this target domain \mathbb{T} are unannotated, so the unlabeled target set is initialized by $\mathbb{T}_u = \mathbb{T}$, and the labeled target set is empty as $\mathbb{T}_l = \emptyset$. Before the ASSFT ($r = 0$), the first target samples x_1 with its annotation y_1 is selected to optimize the network as $\mathcal{F}^{(0)}(\Theta)$. This sample is added to the labeled target set as $\mathbb{T}_l = \mathbb{T}_l \cup \{(x_1, y_1)\}$ and removed from the unlabeled target set as $\mathbb{T}_u = \mathbb{T}_u \setminus \{x_1\}$.

Subsequently, the AL procedure is implemented as follows. At the first round $r = 1$, we implement the Active Test Time Sample Query strategy to actively query \mathcal{N}_B instances from the unlabeled target set \mathbb{T}_u for annotation based on their DKD and ASD metric scores. These samples $\mathbf{X}_t^1 = \{x_1, \dots, x_{\mathcal{N}_B}\}$ with their annotations $\mathbf{Y}_t^1 = \{y_1, \dots, y_{\mathcal{N}_B}\}$ are added to the labeled target set $\mathbb{T}_l = \mathbb{T}_l \cup \{(\mathbf{X}_t^1, \mathbf{Y}_t^1)\}$, while the unlabeled target set is updated as $\mathbb{T}_u = \mathbb{T}_u \setminus \{\mathbf{X}_t^1\}$. Subsequently, this labeled target set is utilized to fine-tune the model as $\mathcal{F}^{(1)}(\Theta)$ via Selective Semi-supervised Fine-tuning, which includes three stages. Specifically, the network is fine-tuned as $\mathcal{F}^{(1)}(\Theta)$ by the images $\mathbf{X}_{t,l}^1$ with their annotations $\mathbf{Y}_{t,l}^1$ from the labeled target set \mathbb{T}_l in a fully-supervised manner. Then a number \mathcal{N}_{SU} of unlabeled samples $\mathbf{X}_{t,u}^1 = \{x_1, x_2, \dots, x_{\mathcal{N}_{SU}}\}$ is selected from the unlabeled target set \mathbb{T}_u based on predictive confidence and semantic distance, and the number of selected unlabeled samples is equal to the number of labeled samples in the current iteration r as $\mathcal{N}_{SU} = \mathcal{N}_B \cdot r$. The network $\mathcal{F}^{(1)}(\Theta)$ is employed to generate corresponding pseudo labels $\mathbf{Y}_{t,u}^1 = \{y_1, y_2, \dots, y_{\mathcal{N}_{SU}}\}$. In the third stage, these selected samples $\mathbf{X}_{t,u}^1$ and their pseudo-labels $\mathbf{Y}_{t,u}^1$ are combined with samples from the labeled target set \mathbb{T}_l as a new set $\mathbb{T}_{l,p} = \mathbb{T}_l \cup \{(\mathbf{X}_{t,u}^1, \mathbf{Y}_{t,u}^1); \mathcal{M}_t\}$ to fine-tune the

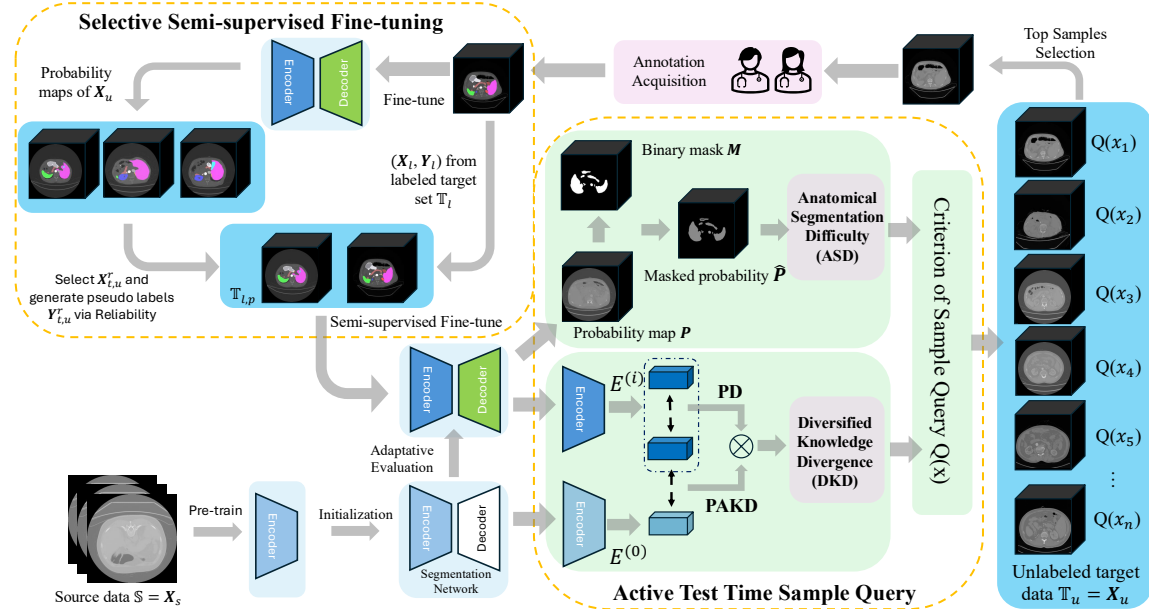


Figure 1: Active Selective Semi-supervised Fine-tuning (ASSFT) of medical vision foundation models for volumetric medical image segmentation. The segmentation network was pre-trained on the source data $\mathbb{S} = \{X_s\}$ and adapted to the target domain \mathbb{T} for downstream evaluation. ASSFT employs an **Active Test Time Sample Query** strategy to evaluate the information level of each target sample. This strategy employs two metrics: **Diversified Knowledge Divergence (DKD)** and **Anatomical Segmentation Difficulty (ASD)**. The scores of these two metrics are combined to form the criterion for sample query $Q(x)$ of unlabeled target data $\mathbb{T}_u = \{X_u\}$. Top samples X_t with large query scores are selected for annotation Y_t by experts. These queried samples and their annotations are used to fine-tune the network via a **Selective Semi-supervised Fine-tuning**. After fine-tuned by labeled data (X_t, Y_t) , the network makes predictions to generate probability maps for unlabeled target data X_u . Unlabeled data $X_{t,u}^r$ are selected and their pseudo labels $Y_{t,u}^r$ are generated. These data $(X_{t,u}^r, Y_{t,u}^r)$ are combined with labeled data (X_t, Y_t) to fine-tune the network.

network $\mathcal{F}^{(1)}(\Theta)$. The AL is implemented in \mathbb{T}_u for the next round. In each subsequent round ($r > 1$), \mathcal{N}_B samples $X_t^r = \{x_1, \dots, x_{\mathcal{N}_B}\}$ are selected for labeling $Y_t^r = \{y_1, \dots, y_{\mathcal{N}_B}\}$ by the Active Test Time Sample Query strategy, generating the updated labeled target set $\mathbb{T}_l = \mathbb{T}_l \cup \{(X_t^r, Y_t^r); \mathcal{M}_t\}$ and unlabeled target set $\mathbb{T}_u = \mathbb{T}_u \setminus \{X_t^r\}$. This updated labeled target set \mathbb{T}_l is utilized to continuously fine-tune the network as $\mathcal{F}^{(r)}(\Theta)$. Then \mathcal{N}_{SU} unlabeled samples $X_{t,u}^r$ are selected for generating pseudo-labels $Y_{t,u}^r$. Then, the network is fine-tuned using the set $\mathbb{T}_{l,p} = \mathbb{T}_l \cup \{(X_{t,u}^r, Y_{t,u}^r)\}$. The iterations will continue until the labeled target samples reach the predefined annotation budgets \mathcal{N}_{AL} or the AL procedure is implemented to the maximal rounds \mathcal{R} . The whole AL procedure is implemented to efficiently fine-tune the network as $\mathcal{F}(\Theta^*)$ with the minimal number of query samples on the target domain \mathbb{T} .

3.2. Active Test Time Sample Query

Our ASSFT method employs an Active Test Time Sample Query strategy to select the most informative samples from target domains for annotation. This strategy utilizes two query metrics to assess the informativeness of target samples, termed Diversified Knowledge Divergence (DKD) and Anatomical Segmentation Difficulty (ASD).

3.2.1. Diversified Knowledge Divergence

To query samples with unlearned knowledge and intra-domain diversity, we propose a sample-level query metric, termed Diversified Knowledge Divergence (DKD). The score of DKD is calculated by measured two terms. The first term aims to measure the knowledge gap between source and target domains. This is measured by identifying source-dissimilar samples from the target domain. This enables the network to better capture target domain-specific information and learn new adaptive knowledge. The second term ensures that the queried samples contribute complementary information by measuring intra-domain diversity. In other words, the goal is to avoid fine-tuning the model using queried samples with large intra-domain similarity, thus encoding overlapping information for the target domain, and diminishing the efficacy of fine-tuning.

The first term aims to measure the knowledge gap between source and target domains, and is referred to as Prior and Adaptive Knowledge Divergence (PAKD). PAKD is calculated by measuring the semantic dissimilarity between feature embedding obtained using the pre-trained encoder $E^{(0)}$ before adaptation and the ones obtained by the latest fine-tuned encoder $E^{(i)}$. For an unlabeled scan $x_u \in \mathbb{R}^{H \times W \times D}$ (H , W , and D represent the height, width, and depth of a volume scan, respectively) in the unlabeled target

set \mathbb{T}_u , the semantic gap is measured using the cosine distance (CosDis) between these feature embeddings $E^{(0)}(x_u)$ and $E^{(i)}(x_u)$:

$$\text{PAKD}(x_u) = \text{CosDis}(E^{(0)}(x_u), E^{(i)}(x_u)) \quad (1)$$

$$= 1 - \frac{E^{(0)}(x_u) \cdot E^{(i)}(x_u)^T}{\|E^{(0)}(x_u)\| \cdot \|E^{(i)}(x_u)\|} \quad (2)$$

The larger PAKD value is, the larger the dissimilarity between the embeddings is and the larger the gap between the source and target domains is. By selecting samples with large gaps, we enable the network to better capture target domain-specific information and learn new adaptive knowledge.

The second term is utilized to measure intra-domain diversity, and is referred to as Pair-wise Dissimilarity (PD). Instead of employing cluster-based diversity sampling methods, our PD is designed as a weighting term that penalizes samples which demonstrate large semantic similarity to samples with large PAKD scores. Specifically, all samples from the unlabeled target set $\mathbb{T}_u = \{X_u\}$ are sorted in a descending order based on the scores of PAKD as $x_u^1, x_u^2, \dots, x_u^c, \dots, x_u^{\mathcal{N}_u}$. Subsequently, the PD term of the sample x_u^c is measured by calculating the cosine distance between the feature embeddings of this sample x_u^c and the feature embeddings of all samples with larger PAKD values $x_u^1, x_u^2, \dots, x_u^{c-1}$. To enhance the importance of PAKD, the cosine distance between any two samples is weighted by the distance of their indices in this sorted array. The weighted cosine distances between the current sample and all other samples are summed and normalized by the total distance to ensure the PD has the same range as PAKD.

$$\text{PD}(x_u^c) = \frac{\sum_{k=1}^{c-1} k * \text{ConDis}(E^{(i)}(x_u^c), E^{(i)}(x_u^{c-k}))}{\sum_{k=1}^{c-1} k} \quad (3)$$

$$= \frac{\sum_{k=1}^{c-1} k * (1 - \frac{E^{(i)}(x_u^c) \cdot E^{(i)}(x_u^{c-k})^T}{\|E^{(i)}(x_u^c)\| \cdot \|E^{(i)}(x_u^{c-k})\|})}{\sum_{k=1}^{c-1} k}. \quad (4)$$

Finally, the DKD for the sample x_u is calculated by multiplying the PAKD value with its PD value as

$$\text{DKD}(x_u) = \text{PAKD}(x_u) \times \text{PD}(x_u). \quad (5)$$

3.2.2. Anatomical Segmentation Difficulty

Samples with complex patterns in anatomical structures may have a high segmentation difficulty level, leading the model to demonstrate large epistemic uncertainty in their predictions. To measure the complexity of anatomical structures of these target structures, we propose an organ-level query metric, termed Anatomical Segmentation Difficulty (ASD). This metric quantifies the difficulty level in sample segmentation by calculating the multi-class predictive entropy. Instead of evaluating segmentation difficulty level in the whole sample, ASD is designed to evaluate it in the foreground region of interest to avoid the noise from background

regions. Additionally, the foreground is extracted adaptively based on the network learning status and AL stage.

Specifically, for an image sample $x_u \in \mathbb{R}^{H \times W \times D}$ from the target unlabeled set \mathbb{T}_u , the network $\mathcal{F}(\Theta)$ generates C probability maps $\mathbf{P}_i \in \mathbb{R}^{H \times W \times D}$ that contain the probabilities of voxels in the sample x_u for each segmentation class: $\mathbf{P} = \{\mathbf{P}_0, \dots, \mathbf{P}_i, \dots, \mathbf{P}_{C-1}\} | i \in \{0, \dots, C-1\}\}$. The segmentation classes include background and the target anatomical structures, so the first probability map \mathbf{P}_0 contains the probability of each voxel to belong to the background.

First, we want to ensure that the background will not contribute to the calculation of the ASD metric. To this end, we determine the mis-segmentation tolerance. This is stricter during the first iteration of our fine-tuning approaches, and is gradually relaxed as iterations increase. This is implemented by adjusting the probabilities of the background through the application of a dynamic temperature scaling function to the predicted probability map of background \mathbf{P}_0 :

$$\mathbf{P}'_0 = \frac{\mathbf{P}_0}{\tau(r)}, \quad (6)$$

where $\tau(r)$ is a dynamic temperature scaling function based on the learning status and AL stage. The value of the dynamic temperature scaling function decreases from 3 in the first round ($r = 1$) to 1.5 in the last round ($r = \mathcal{R}$) as

$$\tau(r) = -\frac{3}{2} \frac{\log r}{\log \mathcal{R}} + 3. \quad (7)$$

This mis-segmentation tolerance is utilized to reduce confidence in the prediction of background regions, thus avoiding false negatives when generating the binary mask. Instead of employing a fixed temperature scaling mechanism, we propose a dynamic temperature scaling function. The value of this function is determined by the learning status and AL stage dynamically, and decreases with the number of AL iteration r . Specifically, at the first several rounds, the segmentation is underperformed, so a larger temperature value is employed to avoid mis-segmented regions when generating binary masks. In contrast, the segmentation performance is improved significantly with AL optimization, a smaller temperature value is utilized to generate accurate masks.

Subsequently, a binary mask $\mathbf{M} \in \mathbb{R}^{H \times W \times D}$ is generated to identify the foreground regions based on the tolerance-adjusted background probability map \mathbf{P}'_0 and the probability maps for target organs $\{\mathbf{P}_1, \dots, \mathbf{P}_{C-1}\}$

$$\mathbf{P}_{max} = \max([\mathbf{P}_1, \dots, \mathbf{P}_{C-1}]), \quad (8)$$

$$\mathbf{M} = \mathbf{1}[\mathbf{P}'_0 < \mathbf{P}_{max}]. \quad (9)$$

Subsequently, the binary mask is applied to these probability maps \mathbf{P} to highlight foreground regions and avoid the influence of noise from background regions, generating foreground masked predictive probability maps $\hat{\mathbf{P}} \in \mathbb{R}^{C \times H \times W \times D}$ as

$$\hat{\mathbf{P}} = \mathbf{P} \odot \mathbf{M}. \quad (10)$$

Lastly, the ASD score for the sample x_u is measured by calculating the entropy of the class probabilities in the foreground regions as

$$\text{ASD}(x_u) = - \sum_{i=0}^{C-1} \hat{\mathbf{P}}_i(x_u) \log \hat{\mathbf{P}}_i(x_u). \quad (11)$$

3.2.3. Criterion of Sample Query

We normalize the DKD and ASD scores for each unlabeled image x_u from the unlabeled target set \mathbb{T}_u via min-max normalization to ensure that the two scores are in the same range

$$\hat{\text{DKD}}(x_u) = \frac{\text{DKD}(x_u) - \min(\text{DKD}(x_u))}{\max(\text{DKD}(x_u)) - \min(\text{DKD}(x_u))}, \quad (12)$$

$$\hat{\text{ASD}}(x_u) = \frac{\text{ASD}(x_u) - \min(\text{ASD}(x_u))}{\max(\text{ASD}(x_u)) - \min(\text{ASD}(x_u))}. \quad (13)$$

To ensure that the DKD and ASD scores are distributed uniformly in the range $[0, 1]$ and to avoid one score overwhelming the other, we apply a uniform Quantile transformation technique:

$$\widehat{\text{DKD}}(x_u) = \text{QuanTrans}(\hat{\text{DKD}}(x_u)), \quad (14)$$

$$\widehat{\text{ASD}}(x_u) = \text{QuanTrans}(\hat{\text{ASD}}(x_u)). \quad (15)$$

We integrate quantile-transformed and unit-normalized DKD and ASD scores into a unified Active Test Time Sample Query selection criterion $Q \in [0, 2]$ as

$$Q(x_u) = \widehat{\text{DKD}}(x_u) + \widehat{\text{ASD}}(x_u). \quad (16)$$

3.3. Selective Semi-supervised Fine-tuning

In the Selective Semi-supervised Fine-tuning, we employ a three-stage approach. In the first stage of the iteration r , we fine-tune the Med-VFM-based network $\mathcal{F}^{(r)}(\Theta)$ by using the actively queried samples with their annotations $\mathbb{T}_l = \{(\mathbf{X}_l, \mathbf{Y}_l); \mathcal{M}_l\}$. This step enables the networks $\mathcal{F}^{(r)}(\Theta)$ to capture more target-specific information and thus improve the quality of segmentation results in target samples.

In the second stage, we select unlabeled samples $\mathbf{X}_{t,u}^r$ from the unlabeled target set \mathbb{T}_u and employ the network $\mathcal{F}^{(r)}(\Theta)$ to generate pseudo labels $\mathbf{Y}_{t,u}^r$. The selection of the samples is based on two metrics, capturing semantic distance and predictive confidence. Unlabeled samples are selected if they demonstrate small semantic distance to labeled samples and fine-tuned Med-VFMs demonstrate high confidence in their probabilistic predictions. Specifically, if one unlabeled sample demonstrates a small semantic distance to labeled samples, it is highly likely that Med-VFMs have learned its semantic patterns by the fine-tuning in the first stage, and they can generate a high-quality predictive result. Additionally, if the network demonstrates high confidence in the probabilistic prediction of an unlabeled sample, it is likely to make an accurate prediction, thus generating a high-quality pseudo label.

Practically, we first propose to calculate model confidence in predictions for all unlabeled samples $\mathbf{X}_u =$

$\{x_1, x_2, \dots, x_u\}$ from the unlabeled target set \mathbb{T}_u via foreground prediction margin. Foreground prediction margin is calculating by measuring the gaps the largest and second largest predictive probabilities in the foreground regions. Specifically, the largest probability map \mathbf{P}_{\max} and a second largest one $\mathbf{P}_{\max}^{(2)}$ are generated from predicted probabilities $\mathbf{P}_c \in \mathbb{R}^{C \times H \times W \times D}$ by extracting the largest and the second largest probabilities for each voxels as

$$\mathbf{P}_{\max}(x_u) = \max \mathbf{P}_c(x_u), \quad (17)$$

$$\mathbf{P}_{\max}^{(2)}(x_u) = \max_{\mathbf{P}_c < \mathbf{P}_{\max}} \mathbf{P}_c(x_u). \quad (18)$$

However, the network demonstrates high confidence in the background voxels, while foreground voxels occupy a small part of the whole image volume. Thus, the predictive confidence in background voxels will overwhelm that in foreground voxels, and involving all voxels into the calculation of voxel-wise margin may over-estimate the sample confidence. To avoid this, a binary predicted mask $\mathbf{M}_c \in \mathbb{R}^{H \times W \times D}$ is generated from predicted probability maps $\mathbf{P}_c \in \mathbb{R}^{C \times H \times W \times D}$ of an unlabeled sample x_u . This binary mask is generated by assigning foreground and background labels to all foreground and background voxels, respectively as

$$\mathbf{M}_c(x_u) = \mathbb{1}[\arg \max_{c \in \{0, 1, \dots, C-1\}} \mathbf{P}_c(x_u) \neq 0]. \quad (19)$$

We apply the binary mask \mathbf{M}_c to highlight the probability of foreground voxels while suppressing the background voxels as

$$\hat{\mathbf{P}}_{\max}(x_u) = \mathbf{P}_{\max}(x_u) \odot \mathbf{M}_c(x_u), \quad (20)$$

$$\hat{\mathbf{P}}_{\max}^{(2)}(x_u) = \mathbf{P}_{\max}^{(2)}(x_u) \odot \mathbf{M}_c(x_u). \quad (21)$$

The confidence $C(x_u)$ of this sample x_u is measured by calculating the voxel-wise margin between the binary-masked largest and second largest probabilities and summed over all voxels v across the whole volume V as

$$C(x_u) = \sum_{v \in V} (\hat{\mathbf{P}}_{\max}(x_u) - \hat{\mathbf{P}}_{\max}^{(2)}(x_u)). \quad (22)$$

If models demonstrate low predictive confidence on samples, they are unlikely to generate accurate predictions on these samples. To reduce the selection burdens in the following steps, we pre-select the top \mathcal{K} samples with high confidence as the candidates \mathbf{X}_k for the next step, while filtering out others based on learning status of the models. The learning status of the models is estimated by averaging the confidence over all unlabeled samples \mathbf{X}_u from the unlabeled target set \mathbb{T}_u as

$$\bar{C} = \frac{\sum_{x_u \in \mathbf{X}_u} C(x_u)}{U}, \quad (23)$$

where U is the number of samples from the the unlabeled target set \mathbb{T}_u . Thus, the number of selected candidates is determined by

$$\mathcal{K} = \frac{\mathcal{N}_{SU}}{\bar{C}/\tau_c}. \quad (24)$$

τ_c is the temperature to reduce the predictive confidence. Subsequently, we create anchors by employing the encoder $E^{(r)}$ of fine-tuned Med-VFMs to generate feature embeddings for queried samples x_l in the labeled set \mathbb{T}_l as $\mathbf{A}^{(r)} = E^{(r)}(x_l)$. This encoder $E^{(r)}$ is also employed to generate feature embeddings from those high confidence candidates $\mathbf{X}_k = \{x_1, \dots, x_k, \dots, x_K\}$ as $\mathbf{F}^{(r)}(x_k) = E^{(r)}(x_k)$. The semantic distance $D(x_k)$ of a sample x_k is measured by calculating the minimal cosine distance between its embeddings and all anchors as

$$D(x_k) = \min_{a \in \mathbf{A}^{(r)}} [\text{CosDis}(\mathbf{A}^{(r)}, \mathbf{F}^{(r)}(x_k))]. \quad (25)$$

We calculate the reliability R for these candidates \mathbf{X}_k based on their predictive confidence C and their semantic distance D as

$$R(x_k) = C(x_k) \times (1 - D(x_k)). \quad (26)$$

Unlabeled samples are selected from \mathcal{K} candidates \mathbf{X}_k for Med-VFMs to generate pseudo labels. To achieve a balance in semi-supervised fine-tuning, the number of selected unlabeled samples is equal to the number of labeled samples $\mathcal{N}_{SU} = \mathcal{N}_B \cdot r$.

In the last stage, we employ Med-VFMs to generate high-quality pseudo labels $\mathbf{Y}_{t,u} = \{y_1, y_2, \dots, y_{t,u}\}$ for these selected unlabeled samples $\mathbf{X}_{t,u} = \{x_1, x_2, \dots, x_{t,u}\}$ with the largest reliability value. These selected samples and their pseudo labels are combined with queried samples as a new set $\mathbb{T}_{l,p} = \mathbb{T}_l \cup \{(\mathbf{X}_{t,u}', \mathbf{Y}_{t,u}'); \mathcal{M}_t\}$ to fine-tune the Med-VFMs in a semi-supervised manner.

3.4. Uninformative Samples Exclusion

In the Selective Semi-supervised Fine-tuning, \mathcal{N}_{SU} unlabeled samples $\mathbf{X}_{t,u}$ are selected. These samples show small semantic distance to labeled samples, and Med-VFMs demonstrate large confidence in their predictions. Thus, these samples demonstrate large overlapping in the information with labeled samples, and querying them is not able to provide high informativeness to Med-VFMs. To reduce the burdens of active querying, we exclude these selected samples from the process of active sample querying in the next AL round.

3.5. The Architecture of Med-VFM-based Segmentation Network

The segmentation network is built as an U-shape encoder-decoder architecture based on CT-FM (Pai et al., 2025). This network has five layers, including a bottleneck and the number of feature maps in each layer was 32, 64, 256, 512, and 1024, respectively. The residual segmentation block was employed to extract features at each layer in the encoder and the decoder, and the number of residual blocks was 1, 2, 2, 4, and 4 in these layers. Each residual block consists of two cascading convolutional layers followed by a batch normalization layers and a ReLU function. The $3 \times 3 \times 3$ convolutional layer with the stride of 2 was utilized to downsample feature maps in the encoder, and the $3 \times 3 \times 3$

transposed convolutional layer was used to upsample the feature maps in the decoder. The skip-connected features from the encoder were fused with those upsampled in the decoder at the same layer via channel-wise addition. At the initial layer, a $3 \times 3 \times 3$ convolutional layer was employed to convert the number of feature maps from the number of input channels to 32. At the final layer, a $1 \times 1 \times 1$ convolution was used to generate the segmentation prediction. The encoder was pre-trained on extensive CT scans without ground truth annotations via self-supervised learning as demonstrated in CT-FM (Pai et al., 2025), and the decoder was initialized by Kaiming initialization on our own (He et al., 2015).

4. Experiments

4.1. Datasets

To evaluate the effectiveness of our methods, we adapted the Med-VFM-based segmentation network to five abdominal multi-organ segmentation datasets with large differences in the number of subjects, imaging modalities, and the number of organs to be segmented.

AMOS2022-CT. The AMOS2022-CT dataset is from the MICCAI 2022 AMOS abdominal multi-organ segmentation challenge (Ji et al., 2022). It consists of 300 abdominal CT volume scans with voxel-level annotations of 15 organ categories, including spleen, right kidney, left kidney, gallbladder, esophagus, liver, stomach, aorta, inferior vena cava, pancreas, right adrenal gland, left adrenal gland, duodenum, bladder, and prostate/uterus. Each CT volume consists of $67 \sim 369$ slices of 512×512 pixels with a slice spacing of $1.25 \sim 5.00$ mm.

FLARE 2021. This dataset is from The Fast and Low GPU memory Abdominal oRgan sEgmentation (FLARE) challenge (Ma et al., 2022). It consists of 361 CT images with voxel-wise annotations of four abdominal organs, including the liver, the kidneys, the spleen, and the pancreas. It demonstrates a large diversity across various centers, vendors, phases, and diseases.

Abdomen Atlas. This dataset includes 9,262 3D CT volumes with pre-voxel annotations of 25 anatomical structures, including 16 abdominal organs, two thorax organs, five vascular structures, and two skeletal structures (Li et al., 2025). These CT volumes were collected from 112 hospitals in 19 countries, generating this multi-center dataset.

AMOS2022-MRI. This dataset is from MICCAI 2022 AMOS abdominal multi-organ segmentation challenge (Ji et al., 2022). It consists of 60 abdominal MR volume scans with voxel-level annotations of 13 organ categories, including spleen, right kidney, left kidney, gallbladder, esophagus, liver, stomach, aorta, inferior vena cava, pancreas, right adrenal gland, left adrenal gland, and duodenum. Since only two cases have annotations of bladder and prostate/uterus, we removed these two labels from this dataset to avoid extreme class imbalance.

Abdominal MRI. This dataset is from the external evaluation of MRAannotator (Zhou et al., 2025). We selected 30

abdominal MR images from external evaluation with voxel-wise annotations of eight anatomical structures, including spleen, right kidney, left kidney, gallbladder, liver, aorta, inferior vena cava, and pancreas.

Scans from all datasets were preprocessed using a standard pipeline. Specifically, the image intensities were clipped at the 5th and 95th percentiles, and then z-score normalization was applied to each volume. Subsequently, scans were cropped to sub-volumes with a specific size. The patch size was $96 \times 160 \times 160$ in the AMOS2022-CT dataset, $96 \times 192 \times 160$ in the FLARE 2021 dataset, $96 \times 128 \times 160$ in the Abdomen Atlas dataset, $48 \times 160 \times 224$ in the AMOS2022-MRI dataset, and $64 \times 192 \times 192$ in the Abdominal MRI dataset.

4.2. Implementation Details

The experiments were implemented using PyTorch¹. A combination of dice loss \mathcal{L}_{Dice} and cross-entropy loss \mathcal{L}_{CE} was used as the loss function. The loss function \mathcal{L} can be formulated between the prediction \hat{y} and the ground truth y as follows

$$\mathcal{L} = \mathcal{L}_{Dice}(\hat{y}, y) + \mathcal{L}_{CE}(\hat{y}, y).$$

Models were trained with a batch size of 2 on NVIDIA Tesla A100 PCI-E Passive Single GPU with 40GB of GDDR5 memory. The AdamW was used as the optimizer. The network was trained for 100 epochs in one-shot initialization. Subsequently, the network was fine-tuned for 800 epochs at each round in the Abdomen Atlas domain, and 400 epochs at each round in the other four domains. The learning rate was initially set to 0.0001, and it decayed with a polynomial learning rate scheduler. During training, data augmentation techniques were implemented to improve model robustness. To be specific, patches were rotated between $[-30, 30]$ along three axes with a probability of 0.2 and then scaled between $(0.7, 1.4)$ with a probability of 0.2. Subsequently, all patches were mirrored along all axes with a probability of 0.5. Zero-centered additive Gaussian noise, with variance drawn from the distribution $U(0, 0.1)$, and brightness adjustments were added to each voxel sample, each with a probability of 0.15. The segmentation performance was evaluated using the dice coefficient score (Dice).

4.3. Active Learning Protocols.

We implemented different active learning protocols for these target sets since they have different segmentation complexity and imaging modalities. In AMOS2022-CT, FLARE 2021, and AMOS2022-MRI datasets, we implemented active domain adaptation to query samples to fine-tune the segmentation network on target domains iteratively. Specifically, the AL procedure in AMOS2022-CT and FLARE 2021 was implemented for five rounds ($\mathcal{R} = 5$), and the query budget was 5% at each round ($\mathcal{N}_B = 5\%$). In AMOS2022-MRI, we queried 5% ($\mathcal{N}_B = 5\%$) samples at each round, and implemented AL querying for six rounds

($\mathcal{R} = 6$) since target samples and pre-training samples have different imaging modalities.

Additionally, in the Abdomen Atlas and Abdominal MRI datasets, we implemented active few-shot learning to query a few samples to fine-tune the segmentation network on target domains. In Abdomen Atlas, we queried 5% ($\mathcal{N}_B = 5\%$) and 10% ($\mathcal{N}_B = 10\%$) samples, respectively. In the Abdominal MRI dataset, we queried 2 samples ($\mathcal{N}_B = 2$) at each round for three rounds, resulting in active 3-shot learning, active 5-shot learning and active 7-shot learning, respectively.

4.4. Comparison with State-of-the-arts

To fully evaluate the effectiveness of our method, we implemented them in two different ways. First, we implemented the **ASSFT** to adapt the network following Algorithm 1, including Active Test Time Sample Query and Selective Semi-supervised fine-tuning. Additionally, we implemented Active Test Time Sample Query (**DKD+ASD**) by querying samples via DKD and ASD to fine-tune the network in a fully supervised learning without Selective Semi-supervised fine-tuning.

Subsequently, we compared our methods with other commonly used active learning strategies, including (1) Random Selection (**RAND**): selecting samples randomly, (2) Entropy (**ENPY**): an uncertainty-based strategy to select samples with highest entropy in predictive probabilities (Wang and Shang, 2014) (3) Least Confidence (**LCON**): an uncertainty-based strategy to select samples with smallest confidence in prediction probability (Li and Sethi, 2006) (4) Minimal Margin (**MMAR**): an uncertainty-based strategy to select samples with smallest margin in predictive probabilities (Wang and Shang, 2014) (5) A Core set approach (**Core-set**): a diversity-based strategy to select samples by solving a set-cover problem (Sener and Savarese, 2018) (6) Batch Active learning by Diverse Gradient Embeddings (**BADGE**): a hybrid uncertainty- and diversity-based strategy to select samples from diverse batches constructed by calculating gradients and running K-Means++ (Ash et al., 2020). Additionally, we compared our methods with an active learning method which was initially proposed for medical image segmentation, termed Suggestive Annotations (**SANN**) (Yang et al., 2017). This is a hybrid uncertainty- and diversity-based strategy to select samples with highest uncertainty in predictive probabilities and lowest semantic similarity. Finally, we compared our methods with other active source-free domain adaptation methods, which have been proposed for medical image segmentation, including (1) the Uncertainty-guided Tiered Self-training (**UGTST**): a hybrid uncertainty- and diversity-based strategy to select samples with large aleatoric uncertainty and low neighboring similarity in 2D prostate segmentation from MR images (Luo et al., 2024) and (2) Cascade Uncertainty Predominance (**CUP**): a hybrid uncertainty- and diversity-based strategy to select patches with low uncertainty and large foreground region in UWF-SLO Vessel Segmentation (Wang et al., 2024b).

¹<http://pytorch.org/>

Table 1

Performance comparison between our ASSFT, DKD+ASD, and other SOTA methods when adapting Med-VFMs to the AMOS2022-CT domain. The performance was evaluated using Dice scores, and the results were reported as Mean \pm SD. **Bold** and underline represent the best and the second best results. Our ASSFT method achieved superior performance than other AL and ADA methods (Lower bound 0%: source-training without target fine-tuning; Upper bound 100%: fully supervised training by all target samples; *: $p < 0.01$ with the Mann-Whitney U test between ASSFT and SOTA methods).

Methods	Lower Bound 0%	Query Budgets (Number of Iterations)					Upper Bound 100%
		5% (r=1)	10% (r=2)	15% (r=3)	20% (r=4)	25% (r=5)	
RAND	0.27 \pm 0.10	73.31 \pm 15.50	77.57 \pm 14.65	79.30 \pm 14.40	81.63 \pm 12.87	82.30 \pm 12.50	93.04 \pm 1.23
ENPY	0.27 \pm 0.10	74.24 \pm 14.53	78.17 \pm 13.73	80.78 \pm 13.43	82.59 \pm 13.63	83.31 \pm 12.05	93.04 \pm 1.23
LCON	0.27 \pm 0.10	73.39 \pm 14.75	77.62 \pm 14.00	80.11 \pm 13.74	82.14 \pm 12.13	82.34 \pm 12.36	93.04 \pm 1.23
MMAR	0.27 \pm 0.10	73.92 \pm 14.99	77.63 \pm 13.89	80.44 \pm 13.05	82.23 \pm 13.00	82.82 \pm 12.00	93.04 \pm 1.23
Core-set	0.27 \pm 0.10	74.42 \pm 14.59	78.55 \pm 13.16	81.11 \pm 12.45	82.73 \pm 12.15	84.04 \pm 11.54	93.04 \pm 1.23
BADGE	0.27 \pm 0.10	75.78 \pm 14.28	79.67 \pm 12.94	82.09 \pm 12.50	83.56 \pm 11.95	84.69 \pm 10.17	93.04 \pm 1.23
SANN	0.27 \pm 0.10	75.48 \pm 14.17	78.99 \pm 12.43	81.88 \pm 11.17	83.11 \pm 10.89	84.45 \pm 10.43	93.04 \pm 1.23
UGTST	0.27 \pm 0.10	75.80 \pm 14.06	80.59 \pm 12.92	82.22 \pm 11.72	83.93 \pm 10.79	85.27 \pm 10.72	93.04 \pm 1.23
CUP	0.27 \pm 0.10	73.92 \pm 14.85	77.88 \pm 13.49	80.69 \pm 13.05	82.25 \pm 12.59	83.10 \pm 11.70	93.04 \pm 1.23
DKD+ASD	0.27 \pm 0.10	78.87 \pm 13.92	82.61 \pm 12.51	84.03 \pm 10.48	85.54 \pm 9.74	86.78 \pm 9.57	93.04 \pm 1.23
ASSFT	0.27 \pm 0.10	80.51* \pm 12.53	84.42* \pm 11.65	85.52* \pm 10.06	86.63* \pm 9.28	87.68* \pm 9.08	93.04 \pm 1.23

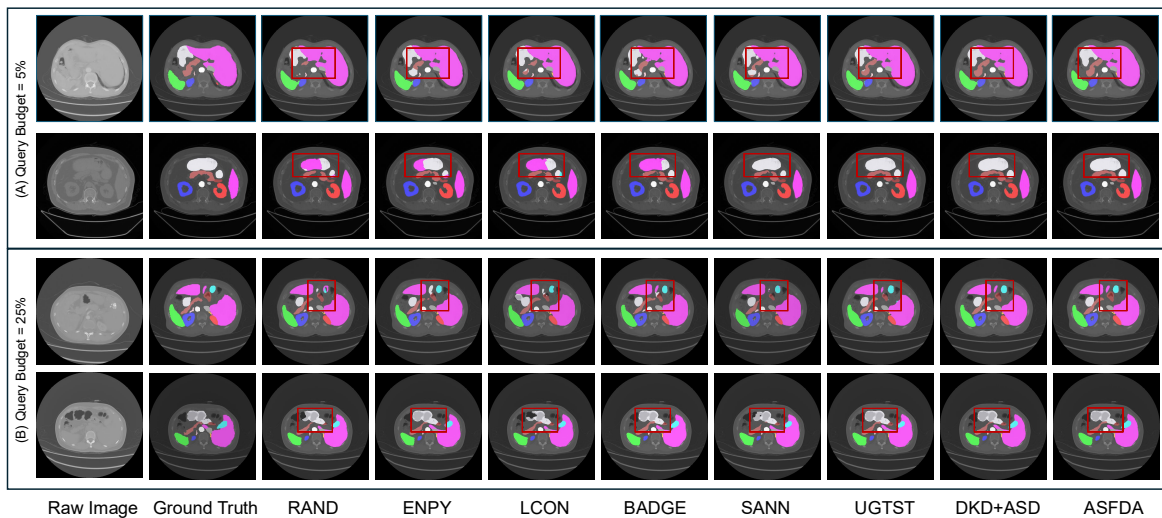


Figure 2: Qualitative comparison among results of the medical vision foundation models fine-tuned by (A) 5% and (B) 25% samples from the AMOS2022-CT domain queried by our methods and other SOTA methods. Red boxes mark the regions where our methods exhibit better segmentation results than SOTA methods.

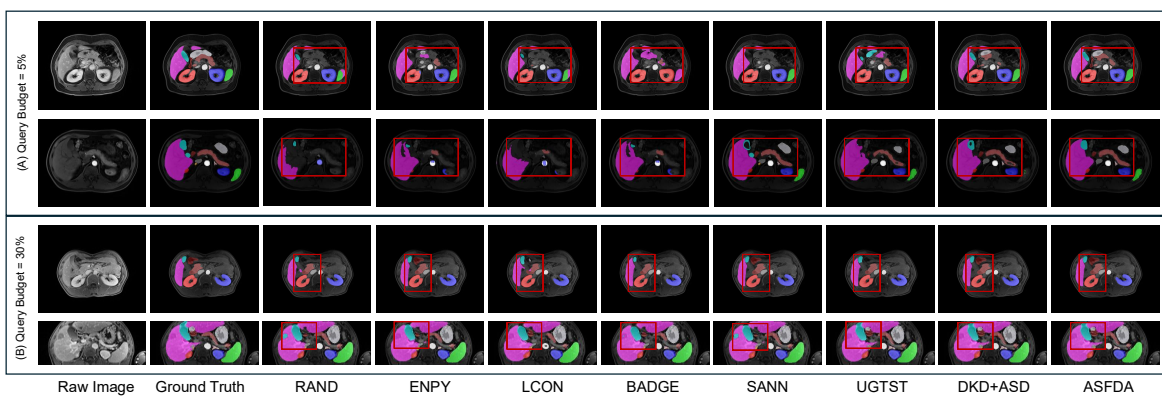


Figure 3: Qualitative comparison among results of the medical vision foundation models fine-tuned by (A) 5% and (B) 30% samples from the AMOS2022-MRI domain queried by our methods and other SOTA methods. Red boxes mark the regions where our methods exhibit better segmentation results than SOTA methods.

Table 2

Performance comparison between our ASSFT, DKD+ASD, and other SOTA methods when adapting Med-VFMs to the AMOS2022-MRI domain. The performance was evaluated using Dice scores, and the results were reported as Mean \pm SD. **Bold** and underline represent the best and the second best results. Our ASSFT method achieved superior performance than other AL and ADA methods (Lower bound 0%: source-training without target fine-tuning; Upper bound 100%: fully supervised training by all target samples; *: $p < 0.01$ with the Mann-Whitney U test between ASSFT and SOTA methods).

Methods	Lower Bound 0%	Query Budgets (Number of Iterations)						Upper Bound 100%
		5% (r=1)	10% (r=2)	15% (r=3)	20% (r=4)	25% (r=5)	30% (r=6)	
RAND	0.46 \pm 0.13	35.84 \pm 27.14	48.06 \pm 25.24	55.28 \pm 21.02	69.15 \pm 14.46	75.56 \pm 12.70	77.98 \pm 11.88	91.32 \pm 3.74
ENPY	0.46 \pm 0.13	40.43 \pm 23.29	58.74 \pm 19.88	71.16 \pm 14.35	76.65 \pm 14.07	78.09 \pm 11.85	80.94 \pm 9.70	91.32 \pm 3.74
LCON	0.46 \pm 0.13	38.05 \pm 25.62	52.12 \pm 24.57	62.35 \pm 18.62	73.78 \pm 13.79	76.12 \pm 12.44	79.29 \pm 11.72	91.32 \pm 3.74
MMAR	0.46 \pm 0.13	38.95 \pm 25.68	55.37 \pm 23.76	63.92 \pm 18.67	75.79 \pm 13.93	77.20 \pm 12.11	80.61 \pm 10.94	91.32 \pm 3.74
Core-set	0.46 \pm 0.13	41.88 \pm 21.56	63.04 \pm 22.01	72.59 \pm 15.91	77.24 \pm 11.02	78.89 \pm 10.03	82.48 \pm 9.18	91.32 \pm 3.74
BADGE	0.46 \pm 0.13	44.00 \pm 21.99	65.49 \pm 19.78	75.65 \pm 13.13	79.30 \pm 10.98	81.31 \pm 10.89	82.80 \pm 8.42	91.32 \pm 3.74
SANN	0.46 \pm 0.13	42.03 \pm 24.73	63.13 \pm 22.63	74.34 \pm 13.42	78.68 \pm 10.70	79.19 \pm 10.74	82.79 \pm 9.54	91.32 \pm 3.74
UGTST	0.46 \pm 0.13	45.29 \pm 21.30	66.14 \pm 19.20	76.45 \pm 12.32	80.86 \pm 10.52	81.86 \pm 10.49	83.53 \pm 8.38	91.32 \pm 3.74
CUP	0.46 \pm 0.13	41.49 \pm 24.83	59.57 \pm 20.87	72.17 \pm 14.89	77.14 \pm 12.85	78.30 \pm 11.17	81.62 \pm 9.12	91.32 \pm 3.74
DKD+ASD	0.46 \pm 0.13	49.31 \pm 20.59	69.66 \pm 18.31	79.52 \pm 11.08	83.37 \pm 10.17	84.25 \pm 9.91	85.18 \pm 8.28	91.32 \pm 3.74
ASSFT	0.46 \pm 0.13	52.06* \pm 18.12	<u>72.06*</u> \pm 17.70	<u>81.59*</u> \pm 10.39	85.74* \pm 9.98	86.13* \pm 9.47	86.90* \pm 7.67	91.32 \pm 3.74

Table 3

Performance comparison between our ASSFT, DKD+ASD, and other SOTA methods when adapting Med-VFMs to the FLARE 2021 domain. The performance was evaluated using Dice scores, and the results were reported as Mean \pm SD. **Bold** and underline represent the best and the second best results. Our ASSFT method achieved superior performance than other AL and ADA methods (Lower bound 0%: source-training without target fine-tuning; Upper bound 100%: fully supervised training by all target samples; *: $p < 0.01$ with the Mann-Whitney U test between ASSFT and SOTA methods).

Methods	Lower Bound 0%	Query Budgets (Number of Iterations)					Upper Bound 100%
		5% (r=1)	10% (r=2)	15% (r=3)	20% (r=4)	25% (r=5)	
RAND	5.86 \pm 0.02	86.70 \pm 9.93	89.74 \pm 6.23	90.57 \pm 5.52	91.56 \pm 5.19	92.05 \pm 4.18	96.85 \pm 1.06
ENPY	5.86 \pm 0.02	88.71 \pm 7.92	91.54 \pm 4.65	92.07 \pm 4.05	92.26 \pm 3.91	93.35 \pm 3.25	96.85 \pm 1.06
LCON	5.86 \pm 0.02	89.70 \pm 6.49	92.05 \pm 5.11	92.91 \pm 3.35	93.74 \pm 2.96	93.83 \pm 2.62	96.85 \pm 1.06
MMAR	5.86 \pm 0.02	89.68 \pm 5.39	92.08 \pm 4.21	92.71 \pm 3.18	93.50 \pm 2.66	93.84 \pm 2.58	96.85 \pm 1.06
Core-set	5.86 \pm 0.02	89.16 \pm 6.46	91.69 \pm 4.23	92.61 \pm 3.75	92.85 \pm 3.05	93.36 \pm 3.19	96.85 \pm 1.06
BADGE	5.86 \pm 0.02	89.51 \pm 5.69	91.77 \pm 4.13	92.65 \pm 3.85	92.99 \pm 3.53	93.80 \pm 2.76	96.85 \pm 1.06
SANN	5.86 \pm 0.02	89.60 \pm 5.44	92.30 \pm 3.80	93.43 \pm 3.15	93.75 \pm 2.92	93.98 \pm 2.91	96.85 \pm 1.06
UGTST	5.86 \pm 0.02	89.56 \pm 5.88	92.15 \pm 3.87	93.26 \pm 3.17	93.60 \pm 2.67	93.70 \pm 3.05	96.85 \pm 1.06
CUP	5.86 \pm 0.02	88.29 \pm 8.87	90.47 \pm 5.39	91.59 \pm 4.38	91.90 \pm 4.20	92.31 \pm 4.12	96.85 \pm 1.06
DKD+ASD	5.86 \pm 0.02	91.65\pm5.09	93.30 \pm 3.68	93.94 \pm 3.08	94.46 \pm 2.78	94.60 \pm 2.53	96.85 \pm 1.06
ASSFT	5.86 \pm 0.02	92.52* \pm 4.31	94.08* \pm 3.27	94.33* \pm 3.04	94.54* \pm 2.64	94.87* \pm 2.47	96.85 \pm 1.06

4.4.1. Experimental results on AMOS2022-CT

We employed our ASSFT method to adapt the Med-VFMs to the AMOS2022-CT domain for volumetric multi-organ segmentation. The fine-tuned network achieved superior performance compared to adaptations using other methods (Table 1 and Figure 2). Specifically, querying 5%-25% of the samples with ASSFT yielded 5-8 points higher Dice score than random sample selection. With only 5% queried samples, ASSFT adapted the network to achieve 80.51 Dice score, improving from 0.27 lower bound performance. Moreover, adapting with 25% queried samples by ASSFT fine-tuned the network to reach over 94% of the upper-bound performance in this domain. These results highlight the effectiveness of ASSFT in adapting Med-VFMs to target segmentation domains.

We further evaluated the Active Test Time Sample Query strategy (DKD+ASD), and it consistently outperformed other active learning query strategies (Table 1 and Figure 2). Specifically, UGTST and SANN leveraged hybrid strategies by evaluating uncertainty and diversity, but our strategy adapted the network to achieve 3-4 points higher Dice score with 5% and 10% queried samples, and 1.5-3 points higher with 25% queried samples. Additionally, compared with diversity-based BADGE and uncertainty-based ENPY, our approach achieved the superior adaptation performance, improving the Dice score by 3-5 points with 5% samples queried.

4.4.2. Experimental results on AMOS2022-MRI

Applying our ASSFT method to adapt the network to the AMOS2022-MRI domain yielded superior performance

compared to other adaptation methods (Table 2 and Figure 3). With 5% samples queried by our ASSFT method, the network achieved an improvement in adaptation performance of more than 51 points in Dice score over the lower-bound performance. Additionally, fine-tuning with 30% of the queried samples by our ASSFT enabled the network to reach over 95% of the upper-bound performance in this domain. Moreover, ASSFT improved the adaptation performance of the network by approximately 16 points of Dice score compared to the adaptation results obtained with 5% randomly queried samples, and by 9 points of Dice score compared to adaptation results obtained with 30% randomly selected samples.

We further evaluated the effectiveness of the Active Test Time Sample Query strategy (DKD+ASD) on the AMOS2022-MRI domain (Table 2 and Figure 3). When querying 5% and 30% of the samples for supervised fine-tuning, our strategy enabled the network to achieve improvements in adaptation performance of more than 13 points and 7 points in Dice score compared to adaptation with 5% and 30% randomly queried samples, respectively. Additionally, querying 5% samples by our strategy for fine-tuning enabled the network to achieve more than 5 points higher Dice score than the diversity-based BADGE strategy. Similarly, querying 5% samples by our strategy demonstrated 4 points higher Dice score than the UGTST. These results demonstrate the effectiveness of the Active Test Time Sample Query strategy (DKD+ASD) in querying informative samples for adaptation of Med-VFMs.

4.4.3. Experimental results on FLARE 2021

Adapting the Med-VFMs to the FLARE 2021 domain with our ASSFT method resulted in superior performance compared to other AL or ADA methods (Table 3 and Figure 4). With 5% of the samples queried, our method increased the network's Dice score by 87 points - from 5.86 (lower bound) to 92.52. Additionally, fine-tuning the network with 25% queried samples by our ASSFT method enabled it to achieve 97.96% of the upper-bound performance in this domain. Compared to random selection (RAND), adaptation by our method yielded a more significant improvement, demonstrating approximately 5.8 points higher Dice score with 5% queried samples. Additionally, ASSFT consistently achieved 1-3 points higher Dice score than LCON and MMAR with 5%-25% of the samples queried.

We also evaluated the Active Test-Time Sample Query strategy (DKD+ASD) on the FLARE2021 domain (Table 3 and Figure 4). Fine-tuning the network with 5%-25% of the samples queried by our strategy achieved 1-2 points higher Dice score than SANN and UGTST. Additionally, with 5% queried samples, our strategy improved the network performance by more than 85 points over the lower-bound performance. Fine-tuning the network with 25% samples queried by our strategy enabled the network to achieve 97.68% of the upper bound performance. These results highlight the effectiveness of our Active Test-Time Sample Query strategy in improving adaptation performance and efficiency.

4.4.4. Experimental results on Abdomen Atlas

Med-VFMs fine-tuned with our ASSFT method achieved superior performance compared to other AL and ADA methods on the Abdomen Atlas domain (Table 4). Specifically, our ASSFT-adapted network reached Dice scores of 83.12 and 84.86 using 5% and 10% queried samples, respectively, representing improvements of approximately 9.4 and 8.1 points over random querying (RAND). While SANN, as a hybrid uncertainty- and diversity-based query strategy, optimized the network to achieve higher Dice score than other AL and ADA methods, our ASSFT method adapted the network to achieve about 3.6 and 3.3 points higher Dice score than SANN with 5% and 10% queried samples, respectively.

When fine-tuned with samples queried by our Active Test-Time Sample Query strategy (DKD+ASD), the network outperformed those adapted with other query methods (Table 4). Specifically, using our query strategy for fine-tuning improved Dice score by 8.2 and 7.1 points with 5% and 10% queried samples, respectively, compared with random selection. Relative to SANN, the gains were about 2.4 and 2.2 points.

4.4.5. Experimental results on Abdominal MRI

When adapting Med-VFMs to the Abdominal MRI domain, our ASSFT method achieved superior performance compared to other AL and ADA methods (Table 5 and Figure 4). The employment of our ASSFT method for active 3-shot learning improved the performance of the source-trained network significantly from approximately 2 to 83.98 Dice points. Additionally, adapted with seven samples queried by our method in active 7-shot learning, the network achieved 88.36 Dice points, demonstrating over 95% of the upper-bound performance (92.95 Dice score). Moreover, the network adapted by our ASSFT method outperformed random querying (RAND) by 17.9, 17.9, and 11.8 points across the three respective adaptation rounds. UGTST was designed to evaluate uncertainty and diversity sequentially, and achieved better performance than other AL and ADA methods. However, our ASSFT method consistently outperformed UGTST by approximately 3-6 Dice points throughout the adaptation process.

The network adapted using samples queried by our Active Test-Time Sample Query strategy (DKD+ASD) also demonstrated superior performance over those optimized with alternative AL and ADA methods in the Abdominal MRI domain (Table 5 and Figure 4). Specifically, the network adapted by our query strategy achieved better performance compared to UGTST- and SANN-adapted networks by approximately 2.5-4 Dice points in the active few-shot learning setting. Additionally, incorporating DKD and ASD metrics to query sample for fine-tuning, the network achieved approximately 15.3, 15.6, and 11.5 higher points in Dice score compared to random querying in active 3-shot, 5-shot, and 7-shot learning, respectively. These results highlight the effectiveness of our ASSFT method and our query

Table 4

Performance comparison between our ASSFT, DKD+ASD, and other SOTA methods when adapting Med-VFMs to the Abdominal Atlas domain. The performance was evaluated using Dice scores, and the results were reported as Mean \pm SD. **Bold** and underline represent the best and the second best results. Our ASSFT method achieved superior performance than other AL and ADA methods (*: $p < 0.01$ with the Mann-Whitney U test between ASSFT and SOTA methods).

Methods	Query Budgets	
	5%	10%
RAND	73.74 \pm 11.98	76.72 \pm 11.48
ENPY	77.39 \pm 10.34	80.46 \pm 9.54
LCON	74.07 \pm 10.66	77.88 \pm 10.90
MMAR	75.74 \pm 11.17	78.33 \pm 9.81
Core-set	79.11 \pm 10.20	81.44 \pm 9.61
BADGE	79.23 \pm 10.01	81.48 \pm 9.52
SANN	79.56 \pm 9.42	81.57 \pm 9.16
UGTST	79.43 \pm 10.15	81.56 \pm 9.75
CUP	77.36 \pm 10.46	79.35 \pm 9.92
DKD+ASD	81.92 \pm 9.31	83.80 \pm 8.70
ASSFT	<u>83.12</u> \pm 8.16	<u>84.86</u> \pm 7.52

Table 5

Performance comparison between our ASSFT, DKD+ASD, and other SOTA methods when adapting Med-VFMs to the Abdominal MRI domain. The performance was evaluated using Dice scores, and the results were reported as Mean \pm SD. **Bold** and underline represent the best and the second best results. Our ASSFT method achieved superior performance than other AL and ADA methods (Lower bound 0%: source-training without target fine-tuning; Upper bound 100%: fully supervised training; *: $p < 0.01$ with the Mann-Whitney U test between ASSFT and SOTA methods).

Methods	Lower Bound 0%	Query Budgets (Number of Iterations)			Upper Bound 100%
		3-shot (r=1)	5-shot (r=2)	7-shot (r=3)	
RAND	2.01 \pm 0.39	66.11 \pm 15.50	69.77 \pm 12.71	76.47 \pm 11.32	92.95 \pm 1.14
ENPY	2.01 \pm 0.39	74.10 \pm 12.77	79.52 \pm 11.78	81.05 \pm 10.12	92.95 \pm 1.14
LCON	2.01 \pm 0.39	75.46 \pm 12.19	80.32 \pm 11.82	82.54 \pm 9.94	92.95 \pm 1.14
MMAR	2.01 \pm 0.39	76.70 \pm 12.25	80.45 \pm 11.20	82.76 \pm 9.93	92.95 \pm 1.14
Core-set	2.01 \pm 0.39	77.94 \pm 11.15	81.62 \pm 10.82	84.21 \pm 9.45	92.95 \pm 1.14
BADGE	2.01 \pm 0.39	77.19 \pm 11.11	81.70 \pm 9.47	84.35 \pm 9.39	92.95 \pm 1.14
SANN	2.01 \pm 0.39	77.48 \pm 10.14	82.13 \pm 8.86	85.34 \pm 8.44	92.95 \pm 1.14
UGTST	2.01 \pm 0.39	78.11 \pm 9.51	82.21 \pm 8.98	85.43 \pm 8.30	92.95 \pm 1.14
CUP	2.01 \pm 0.39	74.92 \pm 12.84	80.22 \pm 11.92	81.95 \pm 10.61	92.95 \pm 1.14
DKD+ASD	2.01 \pm 0.39	81.40 \pm 9.41	85.34 \pm 8.91	87.95 \pm 8.16	92.95 \pm 1.14
ASSFT	<u>2.01</u> \pm 0.39	<u>83.98</u> \pm 8.29	<u>87.63</u> \pm 7.47	<u>88.36</u> \pm 7.32	92.95 \pm 1.14

strategy in improving few-shot adaptation performance compared to other state-of-the-art strategies.

4.5. Ablation study

To evaluate the effectiveness of the two query metrics — DKD and ASD — we conducted ablation studies in which each metric was used to query 5% and 10% of the samples for adapting the network separately to the AMOS2022-CT and AMOS2022-MRI domains.

Table 6

The results of ablation study on DKD metric when adapting Med-VFMs to AMOS2022-CT and AMOS2022-MRI domains. The performance was evaluated using Dice scores, and the results were reported as Mean \pm SD. Adaptation by high DKD samples outperformed those by low DKD samples or randomly selected samples.

Methods	AMOS2022-CT		AMOS2022-MR	
	5%	10%	5%	10%
RAND	73.31 \pm 15.50	77.57 \pm 14.65	35.84 \pm 27.14	48.06 \pm 25.24
High DKD	76.14 \pm 13.67	79.48 \pm 12.56	45.23 \pm 20.89	64.46 \pm 19.56
Low DKD	64.48 \pm 14.72	68.20 \pm 14.83	26.86 \pm 22.67	42.59 \pm 20.75

4.5.1. Ablation on the effectiveness of DKD

We implemented the DKD metric to query the top 5% and 10% highest (High DKD) and lowest (Low DKD) scoring samples for adapting the network to AMOS2022-CT and AMOS2022-MRI domains (Table 6). In the AMOS2022-CT domain, adapting the network by 5% and 10% samples with the highest DKD scores achieved 11-12 points higher Dice score compared to adaptation by samples with the lowest scores. Similarly, in the AMOS2022-MRI domain, adapting the network with the top-5% and top-10% DKD-scoring samples yielded 9-11 higher points Dice score than adaptation with the lowest-scoring samples. Additionally, fine-tuning the network with high-DKD samples consistently achieved better performance than random selection. These results demonstrate that evaluating the DKD metric effectively identifies informative samples, and querying samples with high DKD scores for fine-tuning the network improves adaptation performance compared to random selection.

4.5.2. Ablation on the effectiveness of ASD

To evaluate the effectiveness of the ASD metric in measuring sample informativeness, we adapted the network to the AMOS2022-CT and AMOS2022-MRI domains by querying the top 5% and 10% samples with the highest ASD scores (High ASD) and the lowest ASD scores (Low ASD) (Table 7). Specifically, in both domains, adapting the network with 5% and 10% high ASD samples consistently outperformed adaptation with low ASD samples. Thus, querying samples with high ASD scores effectively identifies the informative samples, and adapting the network with high ASD scores improves the adaptation performance.

We examined the impact of applying binary masks by comparing adaptation performance of our ASD and ENPY. ENPY was employed to query samples with high entropy values which were calculated from the whole samples without applying a binary mask. Adapting the network with high ASD samples outperformed ENPY by approximately 1-3 Dice points in both domains when 5% and 10% samples were queried (Table 7). We further evaluated the impact of the dynamic temperature scaling function by evaluating adaptation performance across different temperature values τ in the ASD metric (Table 7). In both domains, adapting the network with high ASD samples improved the Dice score by 1-1.5 points when the dynamic temperature scaling function

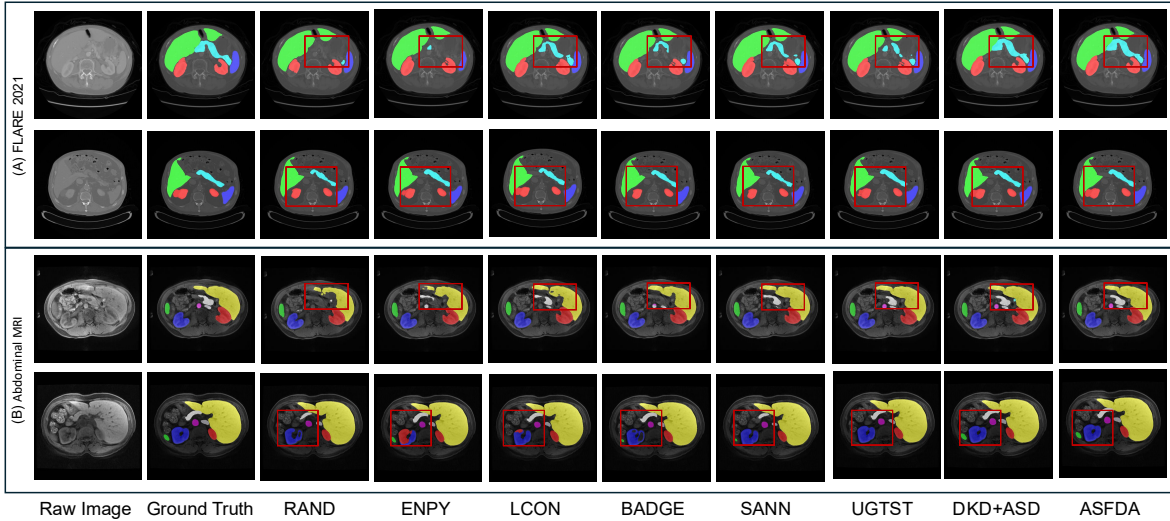


Figure 4: Qualitative comparison among results of the medical vision foundation models fine-tuned by (A) 5% samples from the FLARE2021 domain and (B) 3-shot from the Abdominal MRI domain queried by our methods and other SOTA methods. Red boxes mark the regions where our methods exhibit better segmentation results than SOTA methods.

Table 7

The results of ablation study on ASD metric when adapting Med-VFMs to AMOS2022-CT and AMOS2022-MRI domains. The performance was evaluated using Dice scores, and the results were reported as Mean \pm SD. Adaptation by high ASD samples outperformed those by low ASD samples or entropy-selected samples.

Methods	Temperature function	AMOS2022-CT		AMOS2022-MR	
		5%	10%	5%	10%
ENPY	-	74.24 \pm 14.53	78.17 \pm 13.73	40.43 \pm 23.29	58.74 \pm 19.88
High ASD	$\tau = 1$	75.30 \pm 14.98	79.13 \pm 13.69	42.39 \pm 21.50	61.45 \pm 19.14
Low ASD	$\tau = 1$	62.96 \pm 15.36	63.57 \pm 14.35	29.05 \pm 22.38	39.08 \pm 20.13
High ASD	$\tau(r)$	75.92 \pm 14.39	79.41 \pm 13.24	44.10 \pm 20.41	63.77 \pm 18.48
Low ASD	$\tau(r)$	64.73 \pm 15.44	66.43 \pm 13.88	29.64 \pm 21.35	40.15 \pm 19.49

was applied ($\tau(r)$), compared with ASD querying without temperature scaling ($\tau = 1$). These results demonstrate the effectiveness of incorporating the dynamic temperature scaling function into the ASD metric.

4.5.3. Ablation on Selective Semi-supervised Fine-tuning

The employment of Selective Semi-supervised Fine-tuning enhanced the adaptation performance of Med-VFMs across multiple segmentation domains. For the AMOS2022-CT domain, incorporating this strategy with Active Test Time Sample Query strategy in our ASSFT method improved the performance by approximately 1-2 Dice points (Table 1). When adapting to the AMOS2022-MRI domain with 5%-30% samples queried by our Active Test Time Sample Query strategy (DKD+ASD), Selective Semi-supervised Fine-tuning further improved the performance by 2-3 Dice points (Table 2). Similarly, in the FLARE 2021 domain, employing Selective Semi-supervised Fine-tuning in our ASSFT method improved the segmentation performance of Med-VFMs by approximately 0.5-1 Dice points compared

to the sole use of the query strategy (Table 3). Finally, in Abdomen Atlas and Abdominal MRI domains, applying Selective Semi-supervised Fine-tuning within our ASSFT method improved segmentation performance by approximately 1.2 and 2.5 Dice points, respectively (Table 4 and 5). These results highlight that Selective Semi-Supervised Fine-Tuning provides consistent benefits in adaptation performance of Med-VFMs across diverse domains.

4.6. Analysis on the effectiveness of Selective Semi-supervised Fine-tuning

The goal of the selection mechanism in Selective Semi-supervised Fine-tuning is to select reliable unlabeled samples $X_{t,u}^r$ for generating high-quality pseudo labels $Y_{t,u}^r$ from unlabeled target sets \mathbb{T}_u . To demonstrate the effectiveness of this selection mechanism, we compared the distributions in Dice scores of selected unlabeled samples and unselected unlabeled samples. We adapted the Med-VFMs to the AMOS2022-CT domain for five rounds ($r=1, 2, 3, 4, 5$), and showed dice scores for selected and unselected samples at each round (r1s, r2s, r3s, r4s, r5s, and, r1u, r2u, r3u, r4u, r5u) (Figure 5). The Dice scores of selected unlabeled samples were obviously higher than unselected unlabeled samples at each round.

Second, we implemented Mann-Whitney U test to demonstrate whether the differences in distributions of these two groups were significant (Table 8). The p-values of Mann-Whitney U test were much smaller than 0.01 at each round, demonstrating that the differences of Dice scores between selected and unselected samples were statistically significant. Thus, employing our selection mechanism in Selective Semi-supervised Fine-tuning enables the models to select reliable samples from unlabeled sets for generating high-quality pseudo labels.

Table 8

The p-values of Mann-whitney u test on differences in Dice scores between selected samples and unselected samples in Selective Semi-supervised Fine-tuning when adapting Med-VFMs to the AMOS2022-CT domain.

Query budgets	5% (r1)	10% (r2)	15% (r3)	20% (r4)	25% (r5)
p-values	3.97×10^{-6}	4.53×10^{-13}	5.12×10^{-17}	5.06×10^{-20}	1.80×10^{-22}

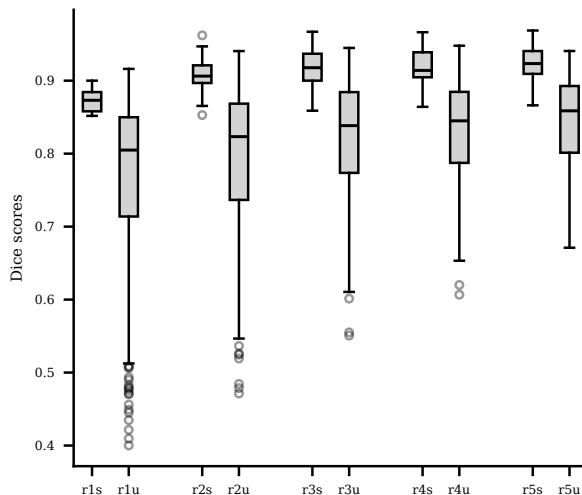


Figure 5: Comparison of distributions of Dice scores from selected (s) unlabeled samples for the Selective Semi-supervised Fine-tuning and unselected (u) unlabeled samples when adapting Med-VFMs to the AMOS2022-CT domain for five rounds (r1, r2, r3, r4, and r5).

5. Conclusion

We proposed the Active Selective Semi-supervised Fine-tuning method to efficiently adapt medical vision foundation models to target domains for volumetric medical image segmentation. This ASSFT method introduces a novel active learning strategy to select the most informative samples from the target domains for fine-tuning Med-VFMs without requiring access to source pre-training samples. It enables high adaptation performance under a minimal sample selection budget. In this AL method, we designed an Active Test Time Sample Query strategy to select samples from the target domains based on two query metrics, termed Diversified Knowledge Divergence and Anatomical Segmentation Difficulty. Additionally, our ASSFT method integrates Selective Semi-supervised Fine-tuning to enhance the performance and efficiency of adaptation. We validated our method by adapting Med-VFMs across five domains for volumetric medical image segmentation. The extensive experimental results demonstrate that our method consistently achieves superior performance compared to state-of-the-art methods.

Declaration of competing interests

The authors declare that they have no known competing financial interests or personal relationships that could have appeared to influence the work reported in this paper.

Acknowledgments

This work was supported by the National Institutes of Health grants U24 CA258483. Computations were performed using the facilities of the Washington University Research Computing and Informatics Facility (RCIF). The RCIF has received funding from NIH S10 program grants: 1S10OD025200-01A1 and 1S10OD030477-01.

CRedit authorship contribution statement

JY: conceptualization, methodology, formal analysis, writing the original draft, reviewing, and editing, visualization; DM: methodology, writing, reviewing, and editing, Funding acquisition, supervision; AS: methodology, writing, reviewing, and editing, supervision.

References

Ash, J.T., Zhang, C., Krishnamurthy, A., Langford, J., Agarwal, A., 2020. Deep batch active learning by diverse, uncertain gradient lower bounds, in: International Conference on Learning Representations.

Du, Z., Li, J., 2023. Diffusion-based probabilistic uncertainty estimation for active domain adaptation. Advances in Neural Information Processing Systems 36, 17129–17155.

Gaillochet, M., Desrosiers, C., Lombaert, H., 2023. Active learning for medical image segmentation with stochastic batches. Medical Image Analysis 90, 102958.

He, J., Liu, B., Yin, G., 2024. Enhancing semi-supervised domain adaptation via effective target labeling, in: Proceedings of the AAAI Conference on Artificial Intelligence, pp. 12385–12393.

He, K., Zhang, X., Ren, S., Sun, J., 2015. Delving deep into rectifiers: Surpassing human-level performance on imagenet classification, in: Proceedings of the IEEE international conference on computer vision, pp. 1026–1034.

Hiasa, Y., Otake, Y., Takao, M., Ogawa, T., Sugano, N., Sato, Y., 2019. Automated muscle segmentation from clinical ct using bayesian u-net for personalized musculoskeletal modeling. IEEE transactions on medical imaging 39, 1030–1040.

Ji, Y., Bai, H., Ge, C., Yang, J., Zhu, Y., Zhang, R., Li, Z., Zhanng, L., Ma, W., Wan, X., et al., 2022. Amos: A large-scale abdominal multi-organ benchmark for versatile medical image segmentation. Advances in neural information processing systems 35, 36722–36732.

Kothandaraman, D., Shekhar, S., Sancheti, A., Ghuhan, M., Shukla, T., Manocha, D., 2023. Salad: Source-free active label-agnostic domain adaptation for classification, segmentation and detection, in: Proceedings of the IEEE/CVF Winter Conference on Applications of Computer Vision, pp. 382–391.

Li, M., Sethi, I.K., 2006. Confidence-based active learning. IEEE transactions on pattern analysis and machine intelligence 28, 1251–1261.

Li, R., Zhang, B., Liu, J., Liu, W., Zhao, J., Teng, Z., 2023a. Heterogeneous diversity driven active learning for multi-object tracking, in: Proceedings of the IEEE/CVF International Conference on Computer Vision, pp. 9932–9941.

Li, S., Zhang, R., Gong, K., Xie, M., Ma, W., Gao, G., 2023b. Source-free active domain adaptation via augmentation-based sample query and progressive model adaptation. IEEE Transactions on Neural Networks and Learning Systems .

Li, W., Yuille, A., Zhou, Z., 2025. How well do supervised 3d models transfer to medical imaging tasks? *arXiv preprint arXiv:2501.11253* .

Li, X., Xia, M., Jiao, J., Zhou, S., Chang, C., Wang, Y., Guo, Y., 2023c. Hal-ia: A hybrid active learning framework using interactive annotation for medical image segmentation. *Medical Image Analysis* 88, 102862.

Luo, Z., Luo, X., Gao, Z., Wang, G., 2024. An uncertainty-guided tiered self-training framework for active source-free domain adaptation in prostate segmentation, in: *International Conference on Medical Image Computing and Computer-Assisted Intervention*, Springer. pp. 107–117.

Ma, J., Zhang, Y., Gu, S., An, X., Wang, Z., Ge, C., Wang, C., Zhang, F., Wang, Y., Xu, Y., et al., 2022. Fast and low-gpu-memory abdomen ct organ segmentation: the flare challenge. *Medical Image Analysis* 82, 102616.

Mahapatra, D., Tennakoon, R., George, Y., Roy, S., Bozorgtabar, B., Ge, Z., Reyes, M., 2024. Alfredo: Active learning with feature disentanglement and domain adaptation for medical image classification. *Medical image analysis* 97, 103261.

Moor, M., Banerjee, O., Abad, Z.S.H., Krumholz, H.M., Leskovec, J., Topol, E.J., Rajpurkar, P., 2023. Foundation models for generalist medical artificial intelligence. *Nature* 616, 259–265.

Nath, V., Yang, D., Landman, B.A., Xu, D., Roth, H.R., 2020. Diminishing uncertainty within the training pool: Active learning for medical image segmentation. *IEEE Transactions on Medical Imaging* 40, 2534–2547.

Ning, M., Lu, D., Wei, D., Bian, C., Yuan, C., Yu, S., Ma, K., Zheng, Y., 2021. Multi-anchor active domain adaptation for semantic segmentation, in: *Proceedings of the IEEE/CVF international conference on computer vision*, pp. 9112–9122.

Pai, S., Hadzic, I., Bontempi, D., Bressem, K., Kann, B.H., Fedorov, A., Mak, R.H., Aerts, H.J., 2025. Vision foundation models for computed tomography. *arXiv preprint arXiv:2501.09001* .

Sener, O., Savarese, S., 2018. Active learning for convolutional neural networks: A core-set approach, in: *International Conference on Learning Representations*. URL: <https://openreview.net/forum?id=H1aIuk-RW>.

Settles, B., 2011. From theories to queries: Active learning in practice, in: *Active learning and experimental design workshop in conjunction with AISTATS 2010, JMLR Workshop and Conference Proceedings*. pp. 1–18.

Shu, X., Li, Z., Tian, C., Chang, X., Yuan, D., 2025. An active learning model based on image similarity for skin lesion segmentation. *Neurocomputing* , 129690.

Siddiqui, Y., Valentin, J., Nießner, M., 2020. Viewal: Active learning with viewpoint entropy for semantic segmentation, in: *Proceedings of the IEEE/CVF conference on computer vision and pattern recognition*, pp. 9433–9443.

Wang, D., Shang, Y., 2014. A new active labeling method for deep learning, in: *2014 International joint conference on neural networks (IJCNN)*, IEEE. pp. 112–119.

Wang, F., Han, Z., Zhang, Z., He, R., Yin, Y., 2023. Mhpl: Minimum happy points learning for active source free domain adaptation, in: *Proceedings of the IEEE/CVF Conference on Computer Vision and Pattern Recognition*, pp. 20008–20018.

Wang, H., Chen, J., Zhang, S., He, Y., Xu, J., Wu, M., He, J., Liao, W., Luo, X., 2024a. Dual-reference source-free active domain adaptation for nasopharyngeal carcinoma tumor segmentation across multiple hospitals. *IEEE Transactions on Medical Imaging* .

Wang, H., Luo, X., Chen, W., Tang, Q., Xin, M., Wang, Q., Zhu, L., 2024b. Advancing uwf-slo vessel segmentation with source-free active domain adaptation and a novel multi-center dataset, in: *International Conference on Medical Image Computing and Computer-Assisted Intervention*, Springer. pp. 75–85.

Wang, S., Safari, M., Li, Q., Chang, C.W., Qiu, R.L., Roper, J., Yu, D.S., Yang, X., 2025. Triad: Vision foundation model for 3d magnetic resonance imaging. *arXiv preprint arXiv:2502.14064* .

Wang, X., Lian, L., Yu, S.X., 2022. Unsupervised selective labeling for more effective semi-supervised learning, in: *European conference on computer vision*, Springer. pp. 427–445.

Wu, T.H., Liu, Y.C., Huang, Y.K., Lee, H.Y., Su, H.T., Huang, P.C., Hsu, W.H., 2021. Redal: Region-based and diversity-aware active learning for point cloud semantic segmentation, in: *Proceedings of the IEEE/CVF international conference on computer vision*, pp. 15510–15519.

Xie, B., Yuan, L., Li, S., Liu, C.H., Cheng, X., 2022. Towards fewer annotations: Active learning via region impurity and prediction uncertainty for domain adaptive semantic segmentation, in: *Proceedings of the IEEE/CVF conference on computer vision and pattern recognition*, pp. 8068–8078.

Yang, C., Huang, L., Crowley, E.J., 2024. Plug and play active learning for object detection, in: *Proceedings of the IEEE/CVF conference on computer vision and pattern recognition*, pp. 17784–17793.

Yang, J., Yu, X., Qiu, P., Marcus, D., Sotiras, A., 2025. Active source-free cross-domain and cross-modality adaptation for volumetric medical image segmentation by image sensitivity and organ heterogeneity sampling, in: *International Conference on Medical Image Computing and Computer-Assisted Intervention*, Springer. pp. 3–12.

Yang, L., Zhang, Y., Chen, J., Zhang, S., Chen, D.Z., 2017. Suggestive annotation: A deep active learning framework for biomedical image segmentation, in: *Medical Image Computing and Computer Assisted Intervention- MICCAI 2017: 20th International Conference, Quebec City, QC, Canada, September 11–13, 2017, Proceedings, Part III 20*, Springer. pp. 399–407.

Zhang, S., Metaxas, D., 2024. On the challenges and perspectives of foundation models for medical image analysis. *Medical image analysis* 91, 102996.

Zhang, W., Lv, Z., Zhou, H., Liu, J.W., Li, J., Li, M., Li, Y., Zhang, D., Zhuang, Y., Tang, S., 2024. Revisiting the domain shift and sample uncertainty in multi-source active domain transfer, in: *Proceedings of the IEEE/CVF Conference on Computer Vision and Pattern Recognition*, pp. 16751–16761.

Zhao, Z., Zeng, Z., Xu, K., Chen, C., Guan, C., 2021. Dsal: Deeply supervised active learning from strong and weak labelers for biomedical image segmentation. *IEEE journal of biomedical and health informatics* 25, 3744–3751.

Zhou, A., Liu, Z., Tieu, A., Patel, N., Sun, S., Yang, A., Choi, P., Lee, H.C., Tordjman, M., Deyer, L., et al., 2025. Mrannotator: multi-anatomy and many-sequence mri segmentation of 44 structures. *Radiology Advances* 2, umaa035.

Zhou, T., Yang, J., Cui, L., Zhang, N., Chai, S., 2024. Sbc-al: Structure and boundary consistency-based active learning for medical image segmentation, in: *International Conference on Medical Image Computing and Computer-Assisted Intervention*, Springer. pp. 283–293.

Zhou, Y., Chia, M.A., Wagner, S.K., Ayhan, M.S., Williamson, D.J., Struyven, R.R., Liu, T., Xu, M., Lozano, M.G., Woodward-Court, P., et al., 2023. A foundation model for generalizable disease detection from retinal images. *Nature* 622, 156–163.

Zhu, W., Huang, H., Tang, H., Musthyala, R., Yu, B., Chen, L., Vega, E., O'Donnell, T., Dehkharghani, S., Frontera, J.A., et al., 2025. 3d foundation ai model for generalizable disease detection in head computed tomography. *arXiv preprint arXiv:2502.02779* .